Torsion Textures Produced by Dynamic Recrystallization in α-Iron and Two Interstitial-Free Steels

J. BACZYNSKI and J.J. JONAS

Two interstitial-free (IF) steels and a high-purity α-iron were deformed in torsion over the temperature range of 600 °C to 840 °C, and the textures produced were measured using conventional X-ray techniques. The conditions were chosen so that dynamic recrystallization (DRX) would take place in the ferrite and static recrystallization would be avoided during cooling after deformation. The DRX textures differ from those observed at room temperature and are dominated by the D1 $(11\bar{2})[111]$, D2 $(\bar{1}\bar{1}2)[111]$, and E2 $(0\bar{1}1)[111]$ components. The D2 becomes increasingly important as the strain is increased, which leads to weakening of the D1 and disappearance of the E2 at large strains. Texture simulations were carried out using a DRX model based on sequential deformation, nucleation, and growth steps. The types of oriented nucleation and selective growth required to reproduce the experimentally observed textures are discussed. The simulations indicate that the low-energy nucleation mechanism plays a dominant role in the formation of bcc DRX textures. The results are also interpreted in terms of the continuous (*in situ*) and discontinuous mechanisms of dynamic recrystallization.

I. INTRODUCTION

THERE have been numerous studies of texture formation during *static* recrystallization in metals. The picture is more complex under dynamic conditions, however, when both deformation and grain boundary migration take place simultaneously. This usually occurs at large strains, which is why torsion testing is the most commonly used experimental technique.

The fundamental processes of recrystallization are nucleation and growth. It has been emphasized by Doherty,[1] Hutchinson,[2] and Humphreys and Hatherly[3] that the classical nucleation theory adopted by Burke and Turnbull[4] from the Johnson–Mehl hypothesis[5] is not valid in the case of recrystallization. The alternative, and commonly accepted, nucleation mechanism involves the preformed nucleus, which means that the regions possessing the new orientations have *already formed* during deformation. At the growth stage of recrystallization, both the stability and mobility conditions must be fulfilled if the nucleus is to be transformed into a new grain.[2]

These processes (nucleation and growth) occur under both static and dynamic conditions and lead to the formation of new preferred orientations. One possible explanation for the development of recrystallization textures is provided by the oriented nucleation theory;[6,7] the latter states that nucleation occurs more easily in some orientations than in others and is, therefore, responsible for the final texture. New arguments for the controlling influence of this mechanism have been published recently in the overview by Hjelen *et al.*[8] By contrast, the selective growth hypothesis[9,10] assumes that some orientations (nuclei of particular orientations) grow much faster than others and are, therefore, largely responsible for the final texture. Such growth selec-

tivity[11,12] is related to the presence of high-mobility boundaries, as discussed by Aust and Rutter[13,14] and Watanabe.[15] It is also generally accepted that only high-angle grain boundaries are able to participate in this process.

The development of bcc torsion textures has been studied, mostly at room temperature.[16–19] Exceptions apply to the work of Montheillet *et al.*,[20] in which high-temperature textures were determined for α-iron. In both cases, however, these results are essentially incomplete, because orientation distribution functions (ODFs) were not employed to describe and analyze the data.

Experimental ODFs of fcc metals undergoing dynamic recrystallization (DRX) have recently begun to be analyzed[21] and simulated numerically.[22] Such experiments or analyses have yet to be reported in the literature for bcc metals. The present study was, therefore, undertaken to determine the relative importance of oriented nucleation and selective growth during DRX in the latter class of materials. An additional aim of this work was to clarify whether the DRX taking place is of the discontinuous or continuous (*in situ*) type. The torsion testing conditions were chosen so that static recrystallization did not take place during cooling after testing. Both optical metallography and texture measurement were carried out, and the ODF results were analyzed in detail. Some DRX texture predictions are presented here. These are based on a new DRX model in which the deformation, nucleation, and growth steps are simulated sequentially.

II. EXPERIMENTAL MATERIALS AND METHOD

Two interstitial-free (IF) steels and a high-purity α-iron were used in the present study. Their chemical compositions and the dimensions of the solid-bar torsion specimens employed are given in Reference 23. A detailed description of the torsion testing machine and the control system are given elsewhere.[24]

Seventeen pass-interrupted torsion tests were performed on the Ti IF and Ti-Nb IF steels in order to establish the

J. BACZYNSKI, Research Associate, and J.J. JONAS, Professor, are with the Department of Metallurgical Engineering, McGill University, Montreal, PQ, Canada H3A 2B2.
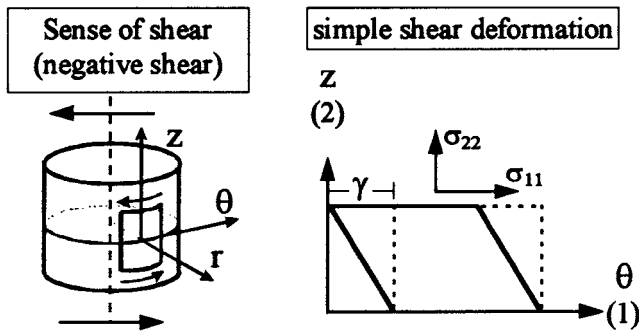Manuscript submitted February 18, 1997.

Fig. 1—Sample reference system in torsion; the pole figures are oriented with respect to the θ-, z-, and r-axes of the sample.

Table I. Some Important Torsion Ideal Orientations*

Orientation	SPN	SD	φ_1	Φ	φ_2
F	$(1\,1\,0)$	$[0\,0\,1]$	180.0	45.0	0.0
D1	$(1\,1\,\bar{2})$	$[1\,1\,1]$	125.3	45.0	0.0
D2	$(\bar{1}\,\bar{1}\,2)$	$[1\,1\,1]$	54.7	45.0	0.0
E1	$(0\,1\,\bar{1})$	$[1\,1\,1]$	39.2	65.9	26.6
E2	$(0\,\bar{1}\,1)$	$[1\,1\,1]$	90.0	35.3	45.0
J1	$(0\,\bar{1}\,1)$	$[\bar{2}\,1\,1]$	30.0	54.7	45.0
J2	$(1\,\bar{1}\,0)$	$[\bar{1}\,\bar{1}\,2]$	150.0	54.7	45.0

*The positive shear convention was used to specify the shear plane normal (SPN) and shear (SD) directions.
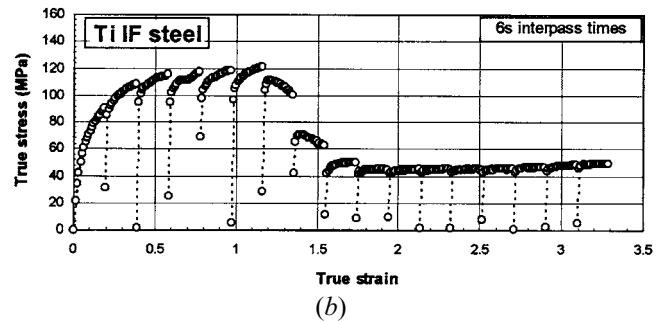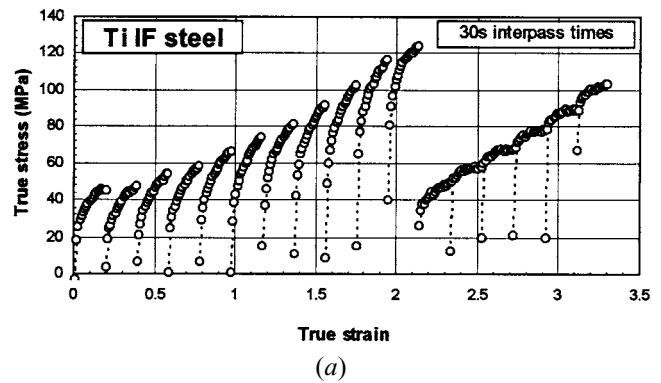

(a)

(b)

Fig. 2—Stress-strain curves determined on the Ti IF steel. The initial temperature was decreased from (a) 1200 °C and (b) 908 °C at a cooling rate of 1 °C/s.

austenite-to-ferrite transformation temperatures. The interpass times were chosen as 6 and 30 seconds, and the temperature was decreased from within the austenite region at a cooling rate of 1 °C/s. Mean flow stresses were calculated for each pass, and the A_{r_1} and A_{r_3} temperatures were determined by the method of Boratto *et al.*[25]

The softening kinetics were measured at 700 °C, 800 °C, and 840 °C in the bcc domain; the latter is about 10 °C below the A_{r_1} temperatures of the two IF steels. A relatively low strain rate of 0.1 s^{-1} was chosen so as to prevent microstructural changes from taking place between the end of a test and the moment when a sample reaches 20 °C. (This is because softening is more rapid after high-strain-rate than low-strain-rate tests.[26]) This elapsed (quenching) time was determined, from measurements made with a thermocouple, to be 3 to 4 seconds, which is equivalent to a cooling rate of 200 °C/s to 270 °C/s. The beginning of static recrystallization in the Ti IF steel (detailed in Section III–A), which corresponds to about 15 pct of softening, was determined to occur after about 12, 17, and 80 seconds after deformation to strains of 19, 6, and 0.5, respectively, at 840 °C. These times are longer (100 seconds after prestraining to 0.3) for the Ti-Nb IF steel and shorter (30 seconds after prestraining to 0.2) for the α-iron. As these times are far longer than the quench times of 3 to 4 seconds, it can be safely concluded that static recrystallization did not take place after the present tests.

Continuous torsion tests were carried out at 600 °C, 700 °C, 800 °C, and 840 °C. Quenched specimens were prepared for texture measurement at increasing strains, as described in detail in Reference 23. Incomplete {110}, {200}, and {211} pole figures were measured on a Siemens D-500 goniometer system, and ODFs were calculated according to the series expansion method introduced by Bunge[27] and dis-

cussed in detail by Van Houtte *et al.*[28] for the case of monoclinic sample symmetry. The orientation of the (θ, z, and r) reference frame employed in pole figure measurement is depicted in Figure 1 and related to the sample axes. The link between the texture coordinate system (shear plane normal and shear direction) and Euler space is specified in Table I.

It should be noted that, in contrast to the methods employed by some researchers, straining was *not* continued during the quenching interval of 3 to 4 seconds. This was done so as to avoid introducing a *deformation* texture, which could obscure some features of the recrystallization textures.

III. EXPERIMENTAL RESULTS

A. *Mechanical Test Results*

Some interrupted flow curves determined on the Ti IF steel over a wide temperature range are presented in Figure 2. Here, the experimental points are marked as open circles. The flow stresses increase rapidly with decreasing temperature in the austenite region. Then, they drop suddenly and again increase with decreasing temperature in the ferrite domain. The transition is sharp, and no flow curve was obtained in the intercritical γ + α region when interpass times of 30 seconds were used (Figure 2(a)) because, during this time interval, the sample cooled right through the two-phase range. By contrast, intercritical flow curves are present in Figure 2(b) when the interpass time is 5 times shorter, this is because less cooling occurs from ''pass'' to ''pass'' under these conditions. As a consequence, the flow curves in the ferrite range for the 6-second interpass times (Figure 2(b)) correspond to much higher temperatures; at these temperatures, much less accumulation of strain is observed.
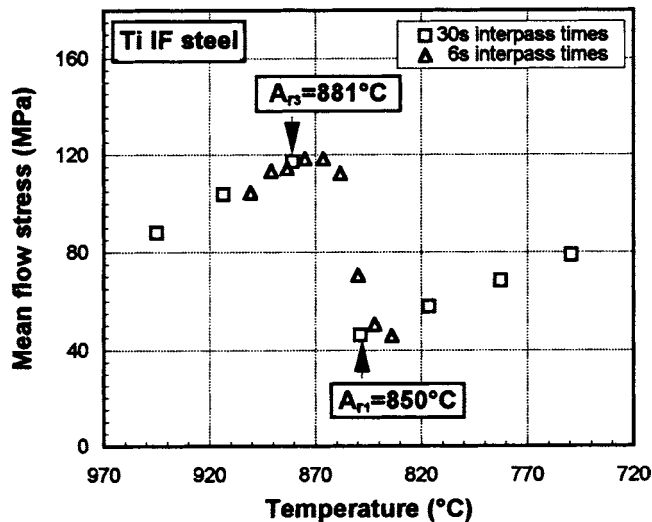
Fig. 3—Determination of the A_{r3} and A_{r1} temperatures for the Ti IF steel.
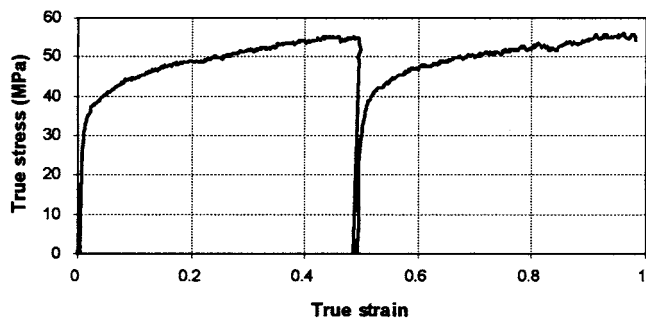

Fig. 4—Measurement of softening in the Ti IF steel at 840 °C, using a strain rate of 0.1/s and a holding time of 1021 s.

Similar remarks apply to the flow curve behaviors applicable to the *ferrite* range in Figure 2. In Figure 2(a), the flow stress increases from about 40 to 100 MPa because the sample temperature decreases by about 180 °C during the six 30-second holding and cooling intervals. By contrast, the flow stress only increases from 40 to about 50 MPa during the nine passes of Figure 2(b), because the temperature decrease is only 54 °C (9×6 s) in this case.

The mean flow stresses $\overline{\sigma} = \frac{1}{\varepsilon} \int \sigma \, d\varepsilon$ (Reference 29), determined from the Ti IF steel data, are displayed in Figure 3. The open squares and triangles represent the experimental points for the 30- and 6-second interpass times, respectively. Note, however, that the 6-second points cover a smaller temperature range than the 30-second points, as already discussed. This method permits identification of the intercritical region and of the A_{r3} and A_{r1} temperatures. The latter were estimated as 881 °C and 850 °C for the Ti IF steel and 889 and 857 °C for the Ti-Nb IF steel. The present work concerns the DRX textures produced *in ferrite*, *i.e.*, below the A_{r1} temperature.
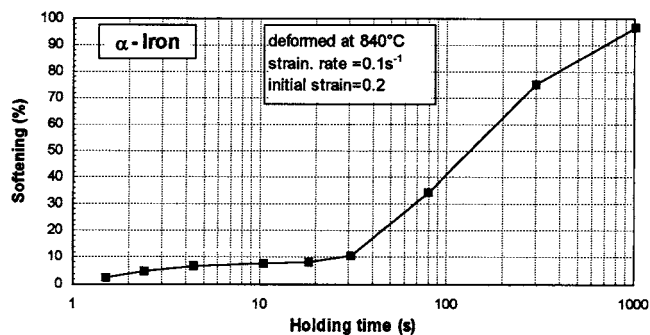
An example of a double-twist test carried out in order to establish the softening kinetics is presented in Figure 4. The fractional softening X (pct) $= (\sigma_M - \sigma_1)/(\sigma_M - \sigma_0)$, per Reference 26, attained a level of about 95 pct in the present example. A series of similar tests were carried out on each of the three ferrous materials, and the interesting ranges of
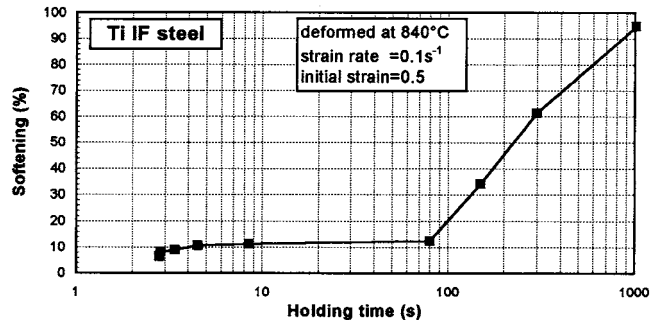
(a)
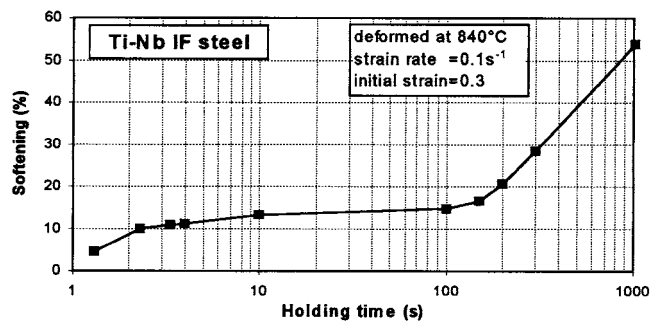
(b)

(c)

Fig. 5—Softening kinetics for the (a) Ti and (b) Ti-Nb IF steel and (c) α-iron based on the data obtained from double twist torsion testing.

softening behavior are displayed in Figures 5(a) through (c). In the case of the Ti IF steel (Figure 5(a)), the amount of softening is low (about 10 to 12 pct) for holding times below 80 seconds. Then, there is a rapid increase in softening, leading to flow properties that are almost fully restored at holding times of about 17 minutes (1021 seconds; Figure 4). Similar behavior was observed in the Ti-Nb IF steel (Figure 5(b)), where the transition point (at which the softening exceeds 10 to 15 pct) was estimated at about 100 seconds. The flow properties were restored by about half (54 pct) at the maximum holding time employed (17 minutes). Restoration is almost complete (97 pct) in the α-iron (Figure 5(c)), under the same testing conditions. In this case, the softening exceeds the relatively low level of about 10 pct after a shorter holding time, which was estimated as 30 seconds.

Some additional results obtained from the softening tests for the Ti IF steel are presented in Figure 6. From this diagram, it is evident that the rate of softening increases with the prestrain. For example, 50 pct softening is attained after 15, 30, and 240 seconds after prestrains of 19, 6, and
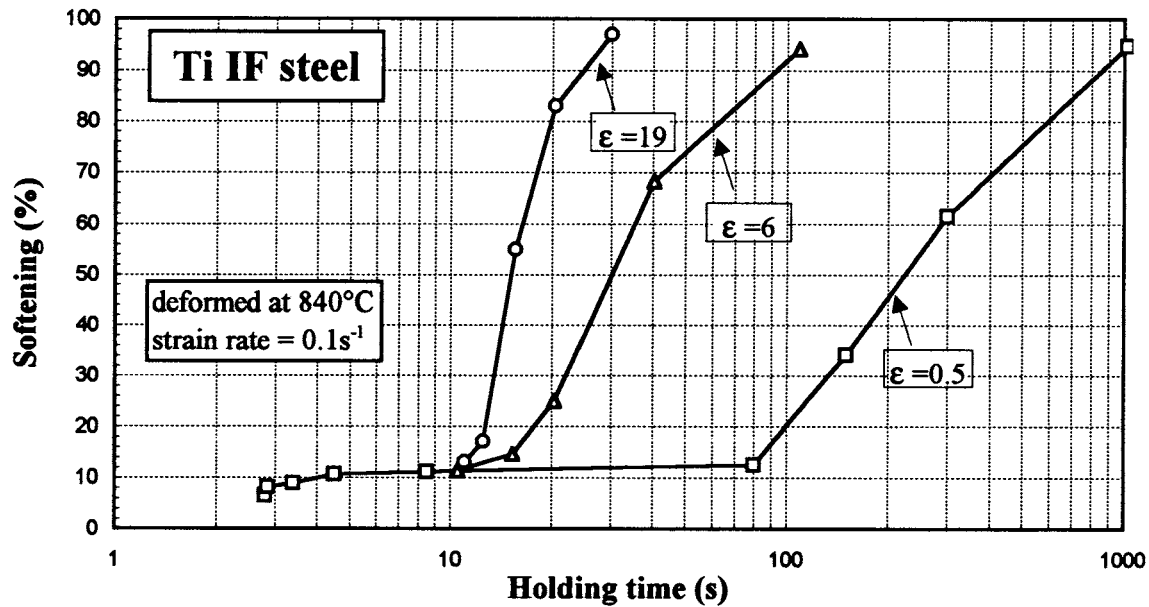
Fig. 6—Softening kinetics for the Ti IF steel deformed to strains of 0.5, 6, and 19 at 840 °C.
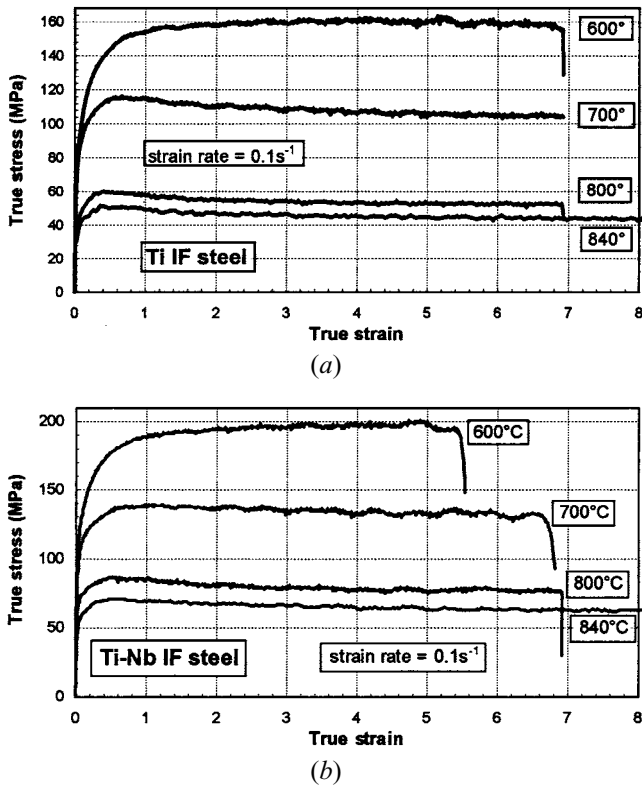

(a)

(b)

Fig. 7—Stress-strain curves for the (a) Ti and (b) Ti-Nb IF steels deformed at elevated temperatures.

0.5, respectively. Similarly, static recrystallization, which corresponds to about 15 pct of softening, is initiated after about 12, 17, and 80 seconds of holding in these cases. These times are significantly longer at the lower experimental temperatures. It can, therefore, be safely concluded that the textures in the present specimens were not affected by static recrystallization. This is because the torsion samples were quenched within time intervals of 3 to 4 seconds.

Some selected $\sigma - \varepsilon$ curves determined on the Ti IF steel are presented in Figure 7(a). Here, a steady state of flow is observed at 600 °C, although it is of interest that this curve does not exhibit a peak or maximum. When the temperature is increased to 700 °C, the flow stress increases with increasing strain, a maximum is reached, and then the flow stress decreases in a constant manner until a steady state of flow is attained. A tendency is observed for the maximum to shift to lower strains as the temperature is increased. Similar trends were observed in the Ti-Nb IF steel (Figure 7(b)), although the flow stresses at the maximum and in the steady-state region are higher in this case than in the Ti IF steel of Figure 7(a). At 840 °C, the ductility was so high that samples of all three materials attained the maximum imposed strain of 25 without failure.

B. *Microstructural Results*

Some typical microstructures produced in the Ti IF steel at room temperature and at 840 °C are presented in Figure 8. The initial grain sizes for both the Ti IF steel (Figure 8(a)) and Ti-Nb IF steel were about 85 μm, while it was 55 μm in the case of the α-iron. After deformation, the initially equiaxed grains were elongated at angles of β deg with respect to the shear direction. This angle decreased with increasing strain to about 15 deg at $\varepsilon = 1.9$ (Figure 8(b)), as called for by the formula tan $2\beta = 2/\gamma$ given by Canova *et al.*[30] A series of microstructures produced in the Ti IF steel at 840 °C are displayed in Figures 8(e) to (f). The average grain size at a strain of 1.9 (Figure 8(c)) was measured as 10 μm. Here, the microstructure is almost fully ''recrystallized.'' A further increase in strain to about 8.8 leads to a microstructure with an average grain size of 12 μm (Figure 8(d)). Again, the grains are equiaxed and their boundaries are sharp. When the still-larger strain of about 19.0 was attained, the microstructure did not change further and the grain size remained about the same (12 μm). Two examples are presented in Figures 8(e) and (f). Here, the ferrite grains are shown at two different magnifications (160
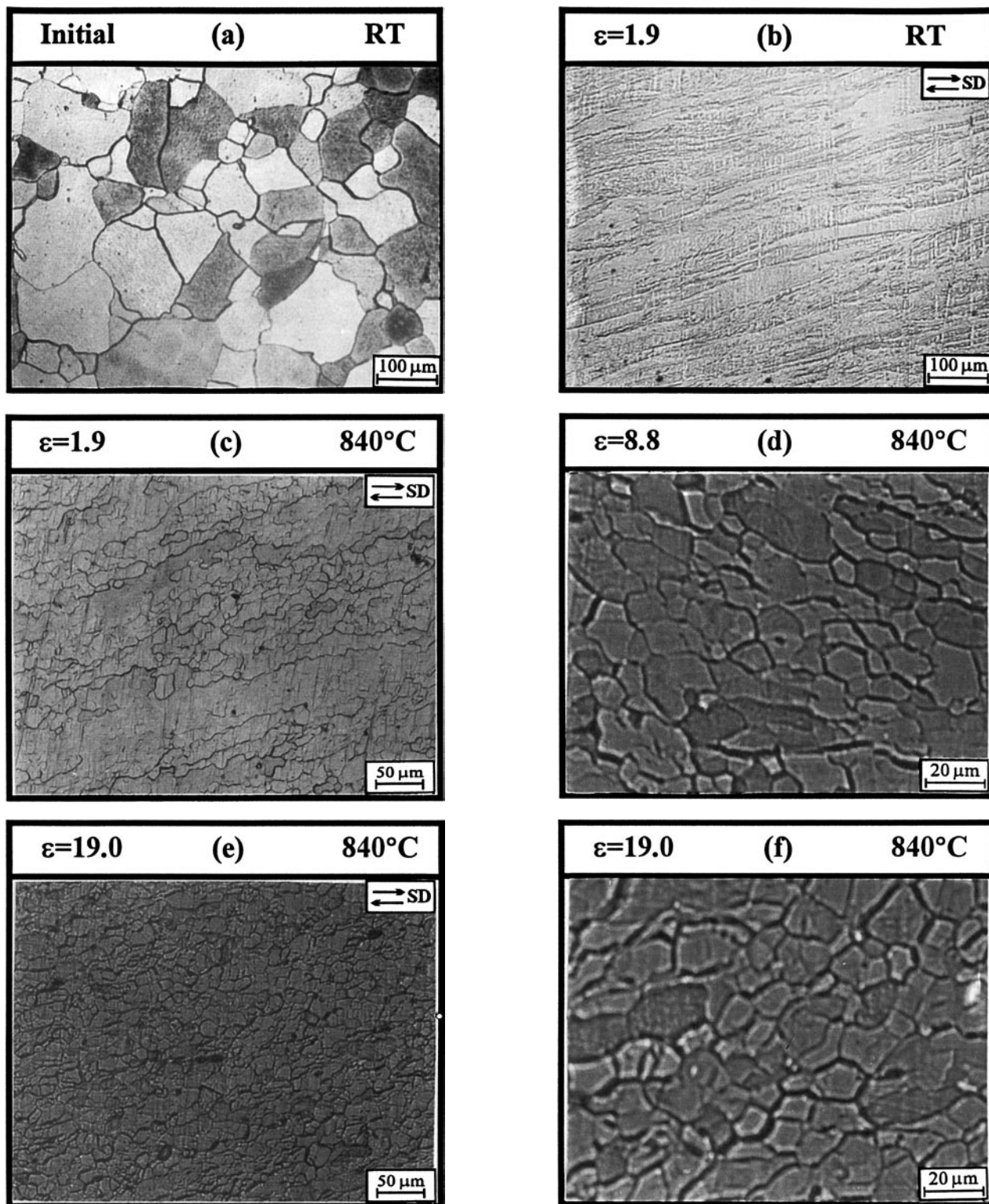
Fig. 8—(*a*) through (*f*) Microstructures produced in the Ti IF steel at room temperature and 840 °C.

and 500 times) in order to provide further details of the grain structure produced under dynamic conditions. This microstructure is representative of all the steady-state strains, as the grain morphology did not change with strain. Similar results were obtained on the Ti-Nb IF steel and the α-iron.

The microstructures obtained at 600 °C, 700 °C, and 800 °C are displayed in Figure 9. Here, it is once more evident that the material is recrystallized; it can also be seen that the grain shape is less and less equiaxed (*i.e.*, it displays more evidence of shear) as the temperature is decreased. By contrast, at temperatures below 600 °C, there is no evidence whatsoever of recrystallization, as typified by Figure 8(b).
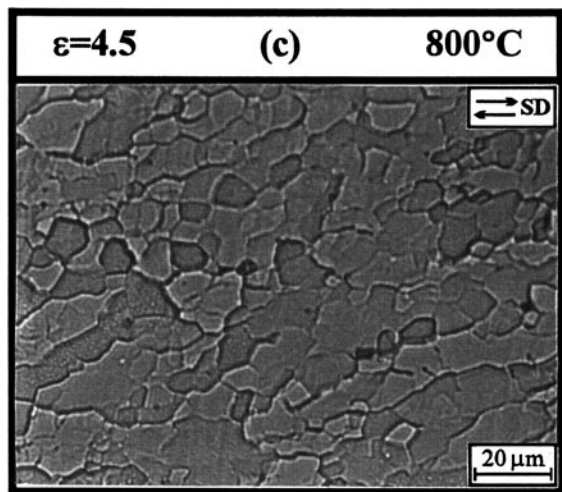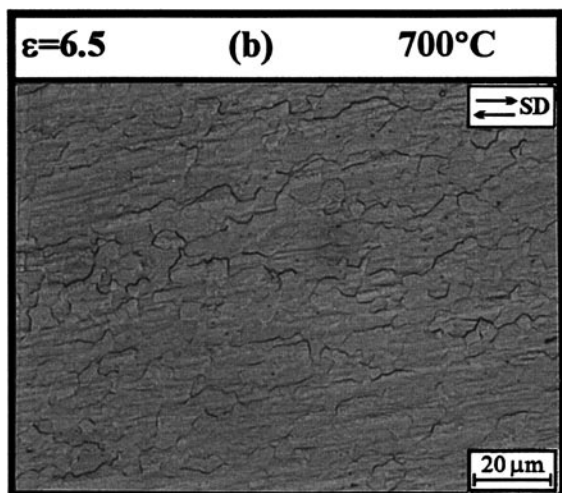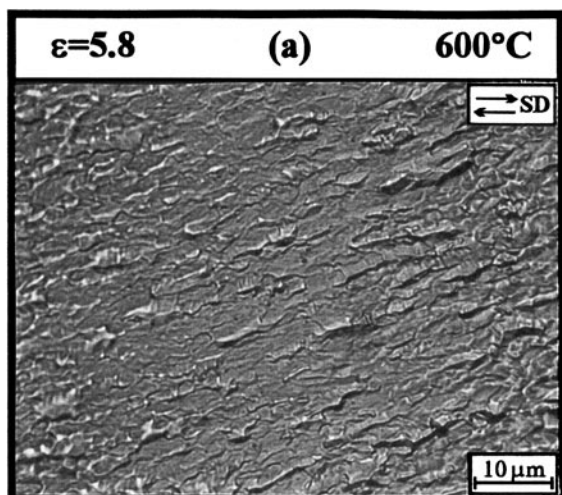
Fig. 9—Microstructures produced in the Ti IF steel at (a) 600 °C, (b) 700 °C, and (c) 800 °C.

C. Texture Results

The full test matrix for texture measurement is presented in Table II. To aid in the analysis of the texture results, some important torsion ideal orientations are identified in Table I. These are specified in terms of the shear plane,

Table II. Matrix of Test Conditions

	T	$\varepsilon \approx$						
	°C	0.5	1.0	2.0	5.0	8–9	19	Maximum*
	400	—	—	—	—	—	—	4.0
	500	—	—	—	—	—	—	3.7
Ti IF	600	—	—	—	—	—	—	5.8
steel	700	—	—	—	—	—	—	6.5
	800	X	X	X	—	—	—	4.5
	840	X	X	X	X	X	X	23.0
	400	—	—	—	—	—	—	3.1
Ti-Nb IF	500	—	—	—	—	—	—	3.6
steel	600	—	—	—	—	—	—	3.5
	840	X	X	X	X	X	—	21.9
α-iron	840	X	—	X	—	X	—	—

  *Just prior to failure.
  X Experiments performed.
  — Not done.

shear direction, and the relevant Euler angles (φ_1, Φ, and φ_2) in the Bunge[27] notation.

The Ti IF steel texture observed at room temperature just prior to failure ($\varepsilon = 4.2$) consists of three main components: the F $\{110\}\langle001\rangle$, J $\{110\}\langle112\rangle$, and D $\{112\}\langle111\rangle$ (Figure 10). The intensities associated with the F, J, D1, D2, and E2 orientations are 5.4, 4.1, 3.7, 4.0, and 2.9, respectively. These preferred orientations are located along the f1, f2, and f3 fibers. Similar results were obtained on the Ti-Nb IF steel and the α-iron.

The ODFs for the Ti IF steel deformed at 600 °C and 700 °C are presented in Figure 11. By comparison with the room-temperature results of Figure 10, it is evident that the texture at 600 °C is twice as intense as the room-temperature textures, and is also qualitatively different. As will be demonstrated in more detail subsequently, DRX begins to operate at 600 °C and is responsible for this change. However, the transition is smooth, and all the features of room-temperature deformation are still clearly recognizable. Hence, this temperature is considered here as the upper limit for the production of bcc deformation textures. The intensities at the F, J, D1, D2, and E2 are 4.0, 3.0, 5.4, 13.7, and 5.8, respectively. These are 0, 0, 5.7, 41.3, and 4.4 for the texture observed at 700 °C just prior to failure ($\varepsilon = 6.5$). In both cases (600 °C and 700 °C), it is evident that the D2 plays an important role during DRX. Similar results were obtained on the Ti-Nb IF steel, and all these observations are also consistent with the data presented by Montheillet et al. in Reference 20.

The DRX textures produced at 840 °C in the Ti IF steel are presented in Figure 12. The typical glide components (F and J) observed at room temperature (Figure 10) are much less significant at 840 °C at a strain of 1.9, and they disappear altogether upon further increases of strain. Here, the important components are the D2 and E1/E2, with intensities of 14.1 and 10.3, respectively. The intensity of the D2 increases to 47.7 as the strain is increased to 4.9 (Figure 12), and those of D1 and E1/E2 remain essentially unchanged. Further increases of strain lead to intensification of the D2 component and to the disappearance of the E1/E2. It should be noted that all the orientations present in the $\varphi_2 = 0$ deg section at $\Phi = 45$ deg are repeated in the $\varphi_2 = 45$ deg section at $\Phi = 90$ deg.
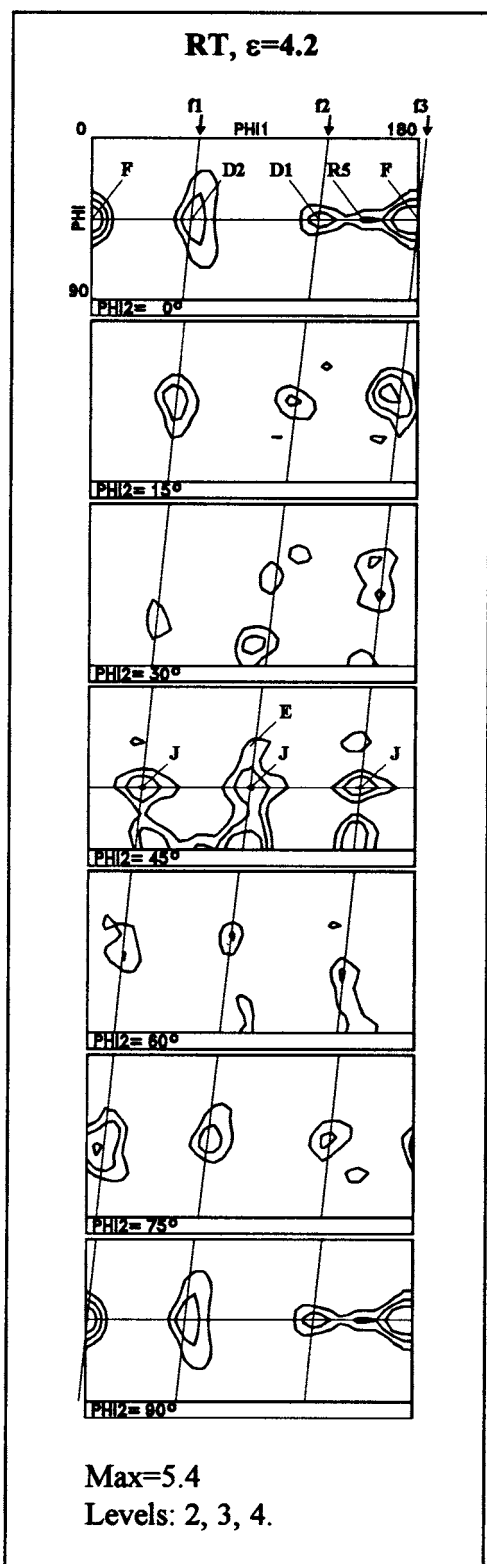
RT, ε=4.2

Max=5.4
Levels: 2, 3, 4.

Fig. 10—Experimental texture of the Ti IF steel deformed in torsion at room temperature.

The textures developed in the Ti-Nb IF steel at room temperature and at 840 °C are similar to those described previously for the Ti IF steel. Two typical examples of the Ti-Nb IF steel textures are shown in Figures 13(a) and (b). It is evident that the experimental ODF of Figure 13(a)

resembles that of Figure 12 at a strain of 1.9. The ODF maximum for the Ti-Nb IF steel at this strain, however, is 11.4. This confirms that niobium addition retards DRX, as discussed in more detail subsequently. No-glide components (F and J) are present at a strain of 8.6 (Figure 13(b)). Instead, a strong D2 component is formed; the D1 intensity is relatively low and the E1 and E2 disappear altogether.

The room-temperature texture produced in the α-iron at a strain of 3.0 (Figure 13(c)) is typical of the three materials investigated in this work (Figure 10). In both cases (Figures 13(c) and 10), all the glide components are present, and the intensities of the F, J1/J2, D1, D2, and E1/E2 components in the α-iron are 4.7, 3.3, 3.1, 3.5, and 3.3, respectively. The DRX texture produced in the α-iron at 840 °C at a strain of 8.2 is illustrated in Figure 13(d). Here, the maximum is 86.9 and the texture is much like the one shown in Figure 13(b) and described earlier. A strong D2 component is formed in the α-iron during DRX, while the glide components (F and J) are consumed by the new orientations and disappear at a strain of 8.2. Further deformation textures are available in References 23 and 31 through 33, while other examples of the DRX textures produced in the present materials are presented in References 32 and 33. Finally, it should be added that the DRX textures produced in two 409 ferritic stainless steels are again similar to those described earlier. These have been reported in Reference 34.

IV. DRX SIMULATION METHOD AND PREDICTIONS

As expected, it was not possible to reproduce the present DRX textures with the aid of a crystal plasticity model based on dislocation glide alone. None of the simulations (carried out within a reasonable range of critical resolved shear stress ratio and rate sensitivity) was successful in causing the F and J components (clearly present from room-temperature to 500 °C; Reference 23) to disappear. It appears, instead, that the DRX texture results from the superposition of deformation, nucleation, and growth mechanisms. These must all be taken into account if the dynamic nature of the process is to be simulated with accuracy. In this work, the simulation procedure is based on the clear separation of the physical mechanisms involved in the formation of DRX textures. The deformation model (described in Reference 23) operates on its own until the critical strain γ_c for DRX is reached. At this point, operation of the nucleation mechanism is initiated and the orientation distribution of the new grains formed in this way is referred to as the nucleation texture. Once the nuclei have formed, they grow into the deformed matrix, giving rise to the growth texture. At this stage of the calculation, two different types of orientation (each with its own volume fraction) are simultaneously present in the sample, so that the final DRX texture consists of a combination of the deformation and growth textures. This combination is then used as the input to the next cycle of the simulation.

Both full- and relaxed-constraint (e_{23} component relaxed) conditions were simulated in the present study, and these were carried out under fixed-end and shortening (2 pct per unit shear) conditions of testing. The volume fraction vol_{DRX} of new DRX grains present at the end of each cycle was set at 12.5 pct. The value of this program parameter was obtained from the relation $vol_{DRX} = 1/(\gamma_{rx}/\Delta\gamma_{DRX})$.
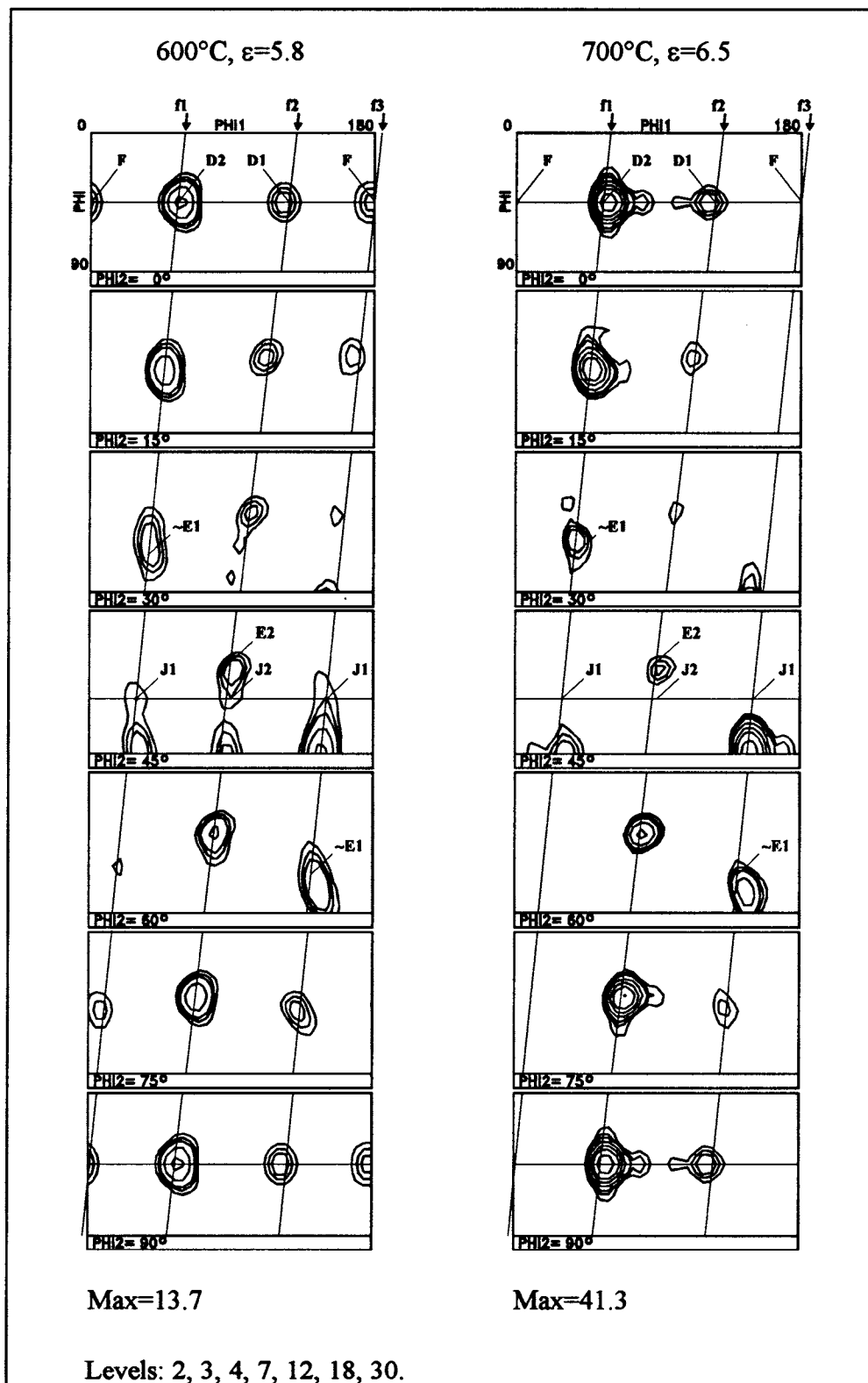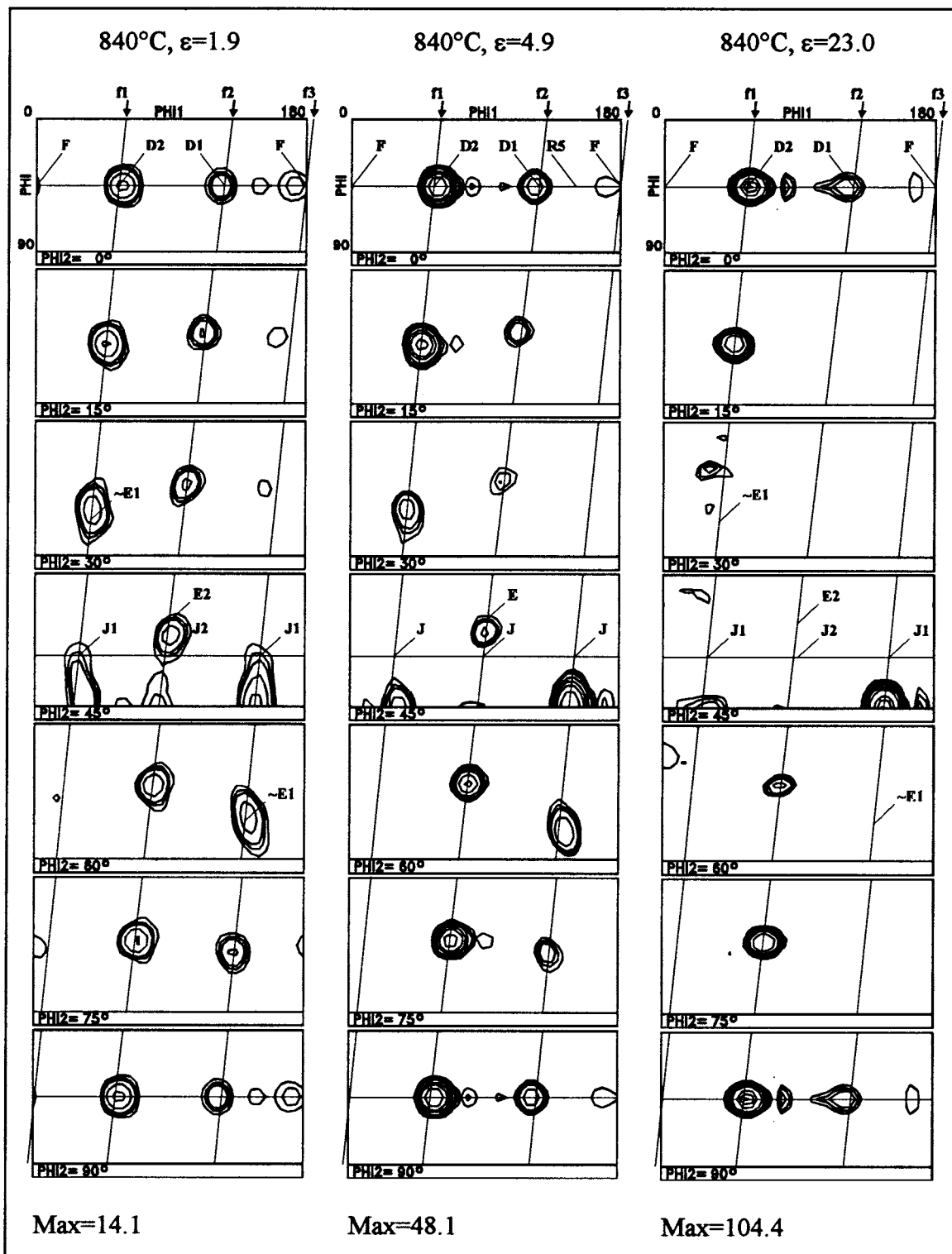
Fig. 11—Textures of the Ti IF steel deformed in torsion at 600 and 700 °C.

Here, γ_{rx} = 2.0 was estimated from the experimental microstructures (*i.e.*, as the strain over which DRX is propagated completely into the material[35]) and $\Delta\gamma_{DRX}$ was set equal to 0.25; *i.e.*, sequences of nucleation and growth were activated after every five increments of shear, where a single increment $\Delta\gamma$ = 5 pct.

The model employed in this work is somewhat similar to those used to simulate static recrystallization.[22,36,37]

Fig. 12—Experimental textures of the Ti IF steel deformed in torsion at 840 °C.

Thus, no account was taken of the temperature, and so no *kinetic* predictions are made.

A. *Nucleation*

Although the nucleus orientations can be random or oriented, only the low-stored-energy hypothesis was employed here, as the other mechanisms did not appear to play important roles, as shown in more detail in Section V. For the present purpose, the low-stored-energy orientations were identified using the Taylor factors generated after each deformation step. These were, therefore, calculated at the end of each recrystallization step. An example of a Taylor factor map obtained from the full constraint theory of crystal plas-
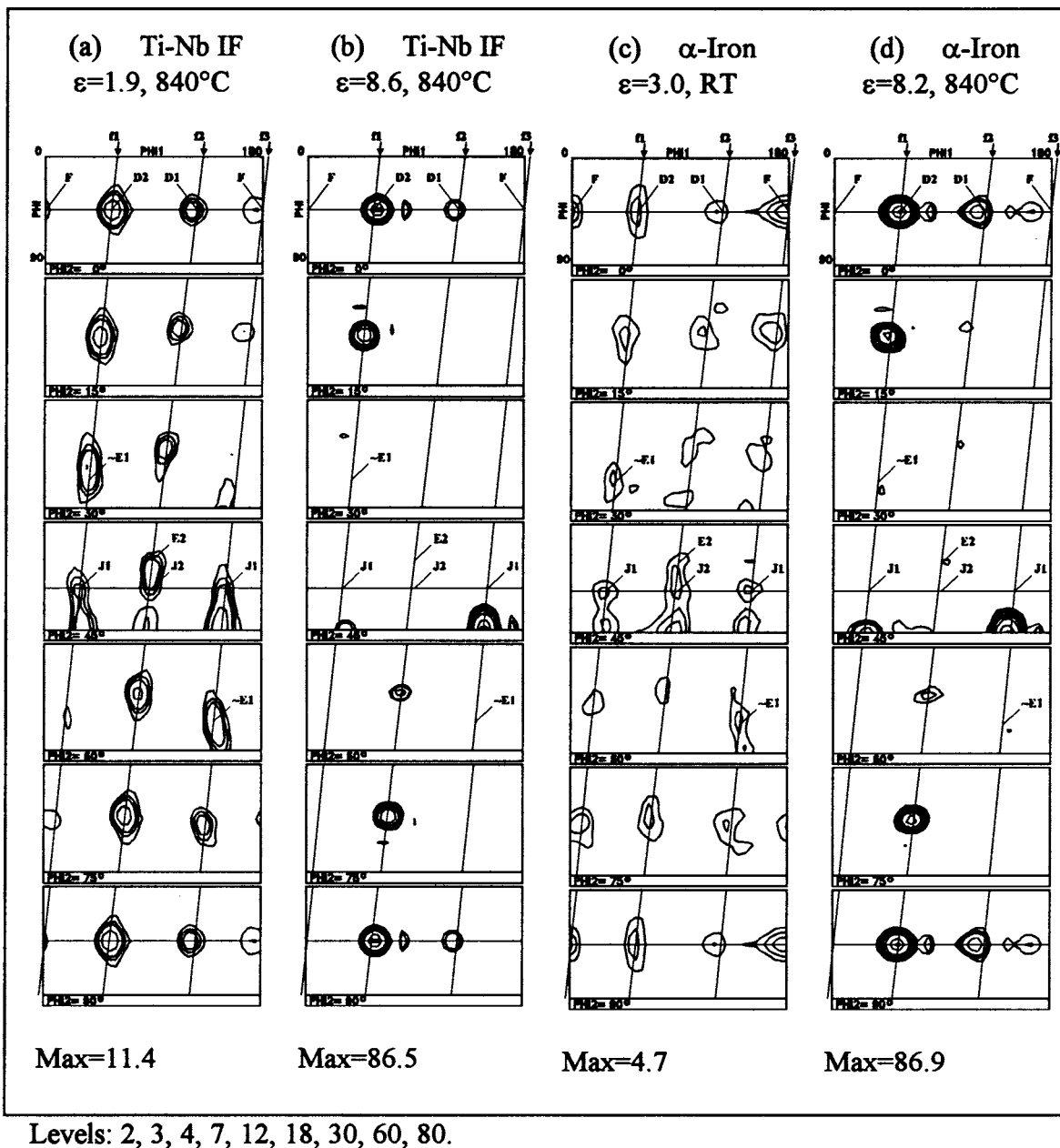
Levels: 2, 3, 4, 7, 12, 18, 30, 60, 80.

Fig. 13—Experimental textures of the (a) Ti-Nb IF steel deformed to a strain of 1.9 at 840 °C, (b) Ti-Nb IF steel deformed to a strain of 8.6 at 840 °C, (c) α-iron deformed to a strain of 3.0 at room temperature, and (d) α-iron deformed to a strain of 8.2 at 840 °C.

ticity is presented in Figure 14. It is evident that, according to this criterion, nucleation can be expected in the vicinities of the D1 (M = 1.77), D2 (M = 1.77), and E2 (M = 1.80) orientations.

Under oriented nucleation conditions, the probability that a nucleus represented by an orientation g_i will be generated can be written as follows:

$$P_{g_i}^N = \exp\left[- \left(\frac{M - M_{min}}{M_0 - M_{min}} \right)^n \right] \qquad [1]$$

Here, n is a Gaussian exponent, M_{min} is the minimum Taylor factor that applies to torsion testing, M_0 is the point above which nucleation is highly unlikely, and M is the Taylor factor of the nucleus g_i of interest. (In the present case, the simulations were carried out with n = 2 and M_0 = 2.4.)

This probability distribution is shown schematically in Figure 15. The volume fraction $f_{g_i}^N$ of this particular orientation that forms can now be written as[36]

$$f_{g_i}^N = c_1 \, P_{g_i}^N \, f_{g_i}^D \qquad [2]$$

where c_1 is a normalization constant and $f_{g_i}^D$ is the volume fraction of orientation g_i present in the deformation texture.

B. *Growth*

There is no unique mathematical description of the growth phenomenon in the literature. Both *uniform* and *selective growth* are possible. Uniform growth is simply represented by the increasing importance of the nucleation texture during DRX, since each nucleus grows uniformly in its surrounding matrix. By contrast, selective growth in-
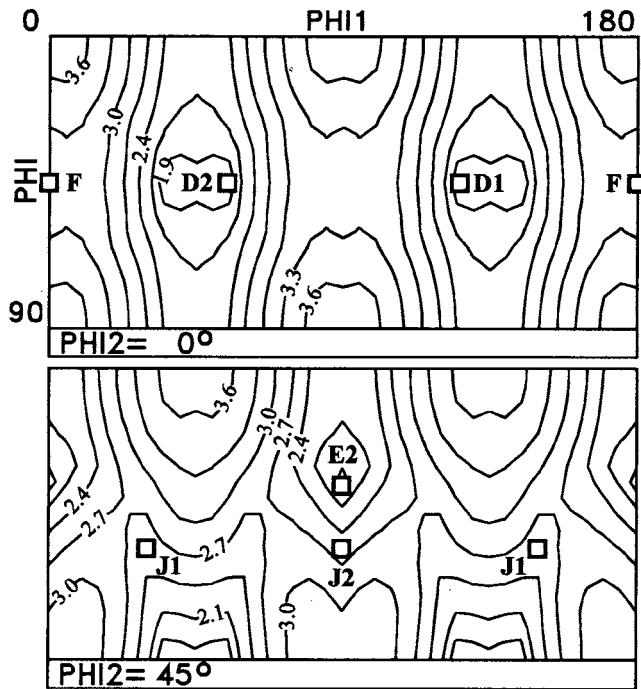
Levels: 1.9, 2.1, 2.4, 2.7, 3.0, 3.3, 3.6

Fig. 14—Full constraint Taylor factor map for torsion. The F, J1/J2, E2, and D1/D2 values are 3.10, 2.53, 1.80, and 1.77, respectively.
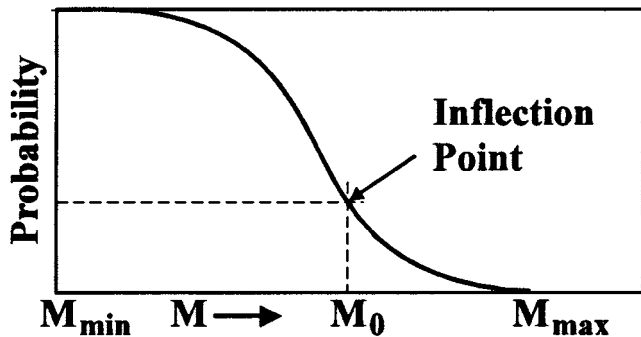

Fig. 15—Taylor factor (M) dependent nucleation law.

Fig. 16—Schematic representation of {110} plane matching growth.[15]
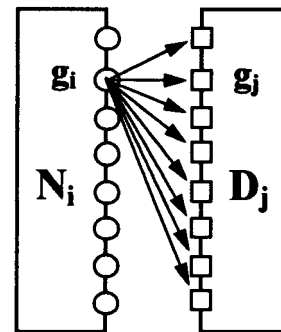
Fig. 17—The nucleus g_i grows into the deformed matrix D_j.

volves the rapid migration of particular grain boundaries. These can be either the {110} plane matching (PM) or the coincidence site lattice boundaries. The former are considered in this article.

The PM concept is illustrated in Figure 16, reproduced from the original work of Watanabe.[15] The two grains (A and B) shown in the figure possess a common ⟨110⟩ axis. Thus, the orientation difference (between grains A and B) can be represented by the misorientation axis-angle pair ⟨110⟩ω. This form of representation is also employed in the present work. It is assumed that when the nucleus and matrix grain possess a common ⟨110⟩ axis (within a certain spread, so as to satisfy the PM condition described subsequently), and when ω exceeds a certain critical value (also discussed subsequently), the nucleus is allowed to grow into the matrix grain.

A general representation of growth is shown schematically in Figure 17. The circles and squares correspond to nuclei and deformed grains, respectively. Nucleus g_i, pres-
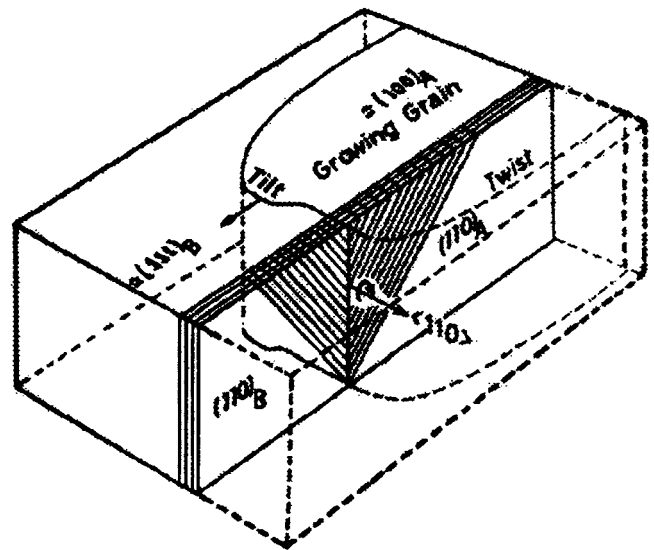
ent in the discrete nucleation texture N_i, grows into the deformed matrix, represented by the discrete deformation texture D_j. This nucleus (of orientation g_i) grows into the j-deformed grains indicated by the arrows. For each N_i-D_j pair, a local growth law is applied that enables the local growth probability $P^L_{\Delta g_{ij}}$ to be evaluated. The average of the local growth probabilities represents the total growth probability $P^G_{g_i}$ that applies to the nucleus g_i growing into the deformed matrix D_j.

The general equations describing the nucleation and growth textures follow the approach originally introduced by Kestens and Jonas[36] for *static* recrystallization, although the formula for the probability of nucleus generation (Eq. [1]) differs slightly from that employed in Reference 36.

C. *Selection Criteria for the Local Growth Probability* $P^L_{\Delta g_{ij}}$

Some physical conditions that affect the growth process are described subsequently. The first criterion was employed to model uniform growth, while the first, second, and third were used to simulate {110} PM growth.

(1) *The critical misorientation angle* ω_c ($\omega_c = 20$ deg). It is generally assumed that a given nucleus g_i cannot readily grow into a deformed grain D_j if the misorientation angle ω between them is less than a critical value ω_c.
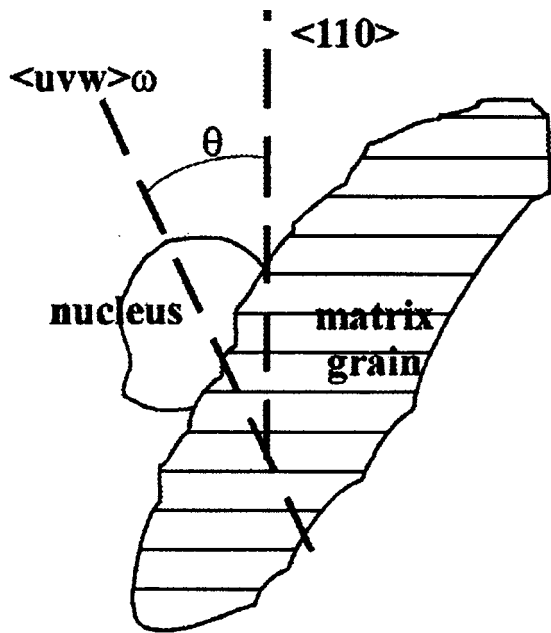
Fig. 18—Schematic representation of the misorientation between an arbitrary combination of a nucleus and a matrix grain. Here, $\langle uvw \rangle \omega$ represents the misorientation axis and angle linking the nucleus to the matrix grain. The $\langle 110 \rangle$ axis that is identified is perpendicular to the most active slip plane in the matrix grain.[27]

$$P^L_{\Delta g_{ij}} = 0 \qquad \text{if } \omega < \omega_c \qquad [3]$$

This condition represents the restricted mobility of low-angle, as opposed to high-angle, boundaries.

(2) *Variant selection*. There are six different {110} slip planes in bcc metals, each containing two different $\langle 111 \rangle$ slip directions. In the variant selection model, it is assumed that the most active {110} slip plane plays an important role in the growth process. The identity of the most active plane is deduced from the deformation model. The single $\langle 110 \rangle$ axis (out of six) that is perpendicular to the most active plane is then selected as the rotation axis.

(3) *The precision of PM*. ''Ideal'' or ''perfect'' PM between a nucleus and a deformed grain occurs when the misorientation axis $\langle uvw \rangle$ corresponds *exactly* to the $\langle 110 \rangle$ axis identified by the variant selection rule $\theta = 0$ (Figure 18). However, generally speaking, the match is not perfect, and a specific allowable range must be allocated to the mismatch. It should be noted that the misorientation axis-angle pair $\langle uvw \rangle \omega$ is calculated to take into account both the sample and crystal symmetries. There are 48 such axis-angle $\langle uvw \rangle \omega$ pairs, in general, and there are 48 symmetrically equivalent angles θ between the misorientation axis $\langle uvw \rangle$ and the selected $\langle 110 \rangle$ axis (Figure 18). The minimum angle θ_{min} ''is a measure of the departure from perfect plane matching between the nucleus and the matrix grain.''[37] Departures from perfect PM were taken into account by the method of Reference 36; this involves the use of a Gaussian function $\exp [-(\theta_{min}/\theta_0)^n]$ in order to evaluate the local growth probability, with a characteristic width $\theta_0 = 2$ deg and an exponent $n = 2$ in the present case.

In the former case, referred to here as uniform growth,

the growth rate does not involve any special relationship between the orientations of the nucleus and the matrix grain. In other words, each nucleus g_i grows into a deformed matrix grain g_j (Figure 17) with the same local growth probability.

$$P^L_{\Delta g_{ij}} = \text{constant} \qquad [4]$$

For simplicity, this constant was set equal to 1. The average of the local growth probabilities represents the total growth probability $P^G_{g_i}$ that applies to the nucleus g_i growing into the deformed matrix D_j.[36]

$$P^G_{g_i} = \sum_j P^L_{\Delta g_{ji}} f^D_{g_j} \qquad [5]$$

and the volume fraction of the growing nucleus was calculated as

$$f^G_{g_i} = c_2 \left(P^G_{g_i} \right)^p f^N_{g_i} \qquad [6]$$

Here, $f^N_{g_i}$ is the volume fraction of nuclei of orientation g_i, c_2 is another normalization constant, and the exponent p represents the relative importance of the nucleation and growth processes. In all the calculations, the normalization procedure described in Reference 36 was employed.

C. *Textures Produced under Simulated DRX Conditions*

The use of oriented nucleation and {110} PM selective growth led to the textures displayed in Figure 19. Here, relaxed constraint and shortening conditions were imposed on the polycrystal in order to reproduce the small amount of shortening (2 pct) observed experimentally. Under these conditions, the E2 and J2 components are the most intense by the time a strain of 2.0 is reached. At this stage of the simulation, the F component has disappeared and only the J2 remains by the time a strain of 5.0 is attained. However, this prediction diverges significantly from the experimental observations (compare the simulated $\varepsilon = 5.0$ texture of Figure 19 to the experimental $\varepsilon = 4.9$ texture of Figure 12). As a result, selective growth was not judged to be important in the formation of the DRX textures produced under the present conditions.

When the deformation of bcc crystals was simulated under *relaxed constraint* and shortening conditions, oriented nucleation and uniform growth led to the DRX textures shown in Figure 20. These predictions agree quite well with the experimental observations. In this case, the intensities of the F and J deformation components are 1.9 and 4.8, respectively, at $\varepsilon = 0.8$, while those of the D1, D2, and E2 are 3.1, 5.7, and 3.7. The D1, D2, and E2 intensities initially increase with strain, while those of F and J decrease to zero at $\varepsilon = 5.0$. At very large strains of about 22.5, the E2 disappears and the D2 dominates, together with the D1, as is evident from the $\varphi_2 = 45$ deg and $\varphi_2 = 0$ deg sections.

V. DISCUSSION

A. *Transition from the Room-Temperature Behavior to the DRX State*

Taking the $\varepsilon = 4.2$ room-temperature texture of the Ti IF steel as an example (Figure 10), it can be seen that the
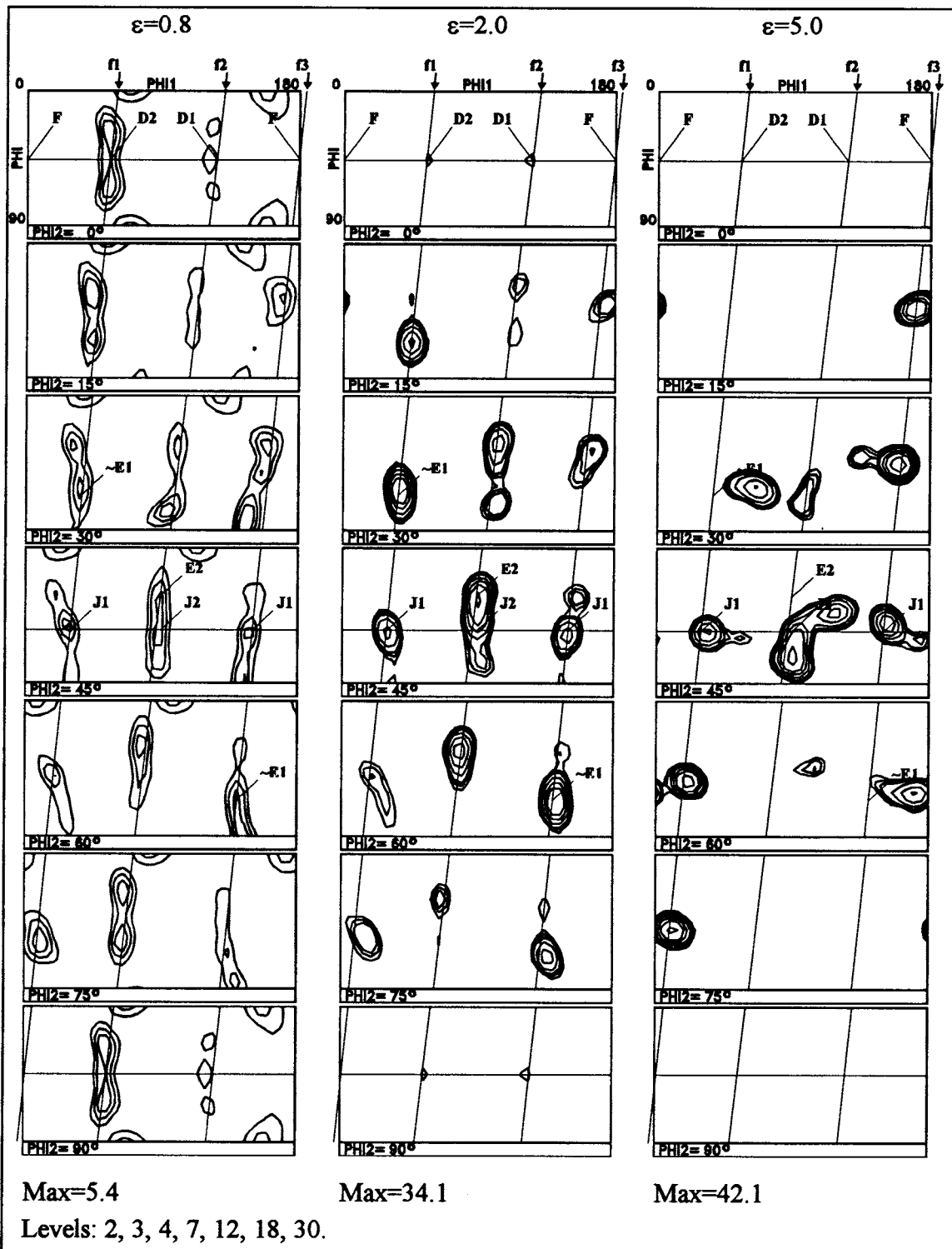
Fig. 19—Simulated ODFs for the oriented nucleation and plane matching case. RC and shortening (2 pct) conditions (e_{23} component relaxed, $\alpha_s = \alpha_h = 0.95$, $\Delta\gamma = 0.05$, and $\Delta\gamma_{DRX} = 0.25$).

F, J1, and J2 components are the most intense, as these are produced by glide. Similar results (Reference 23) were obtained at 400 °C and 500 °C. The increase in the intensities of the D1/D2 and E1/E2 components at 600 °C (Figure 11), especially the development of strong D2 and E2 orientations, originates from the initiation of DRX. This process (DRX) is in its early stages at this temperature, since all the important glide components are still clearly recognizable under the present conditions.

The ''transition'' or ''boundary'' textures are associated with the changes observable on the $\sigma - \varepsilon$ curves of Figure 2 from Reference 23 and Figure 7(a) of this work. The rate of work hardening decreases with increasing temperature, leading to an extensive steady-state region at 600 °C (Fig-
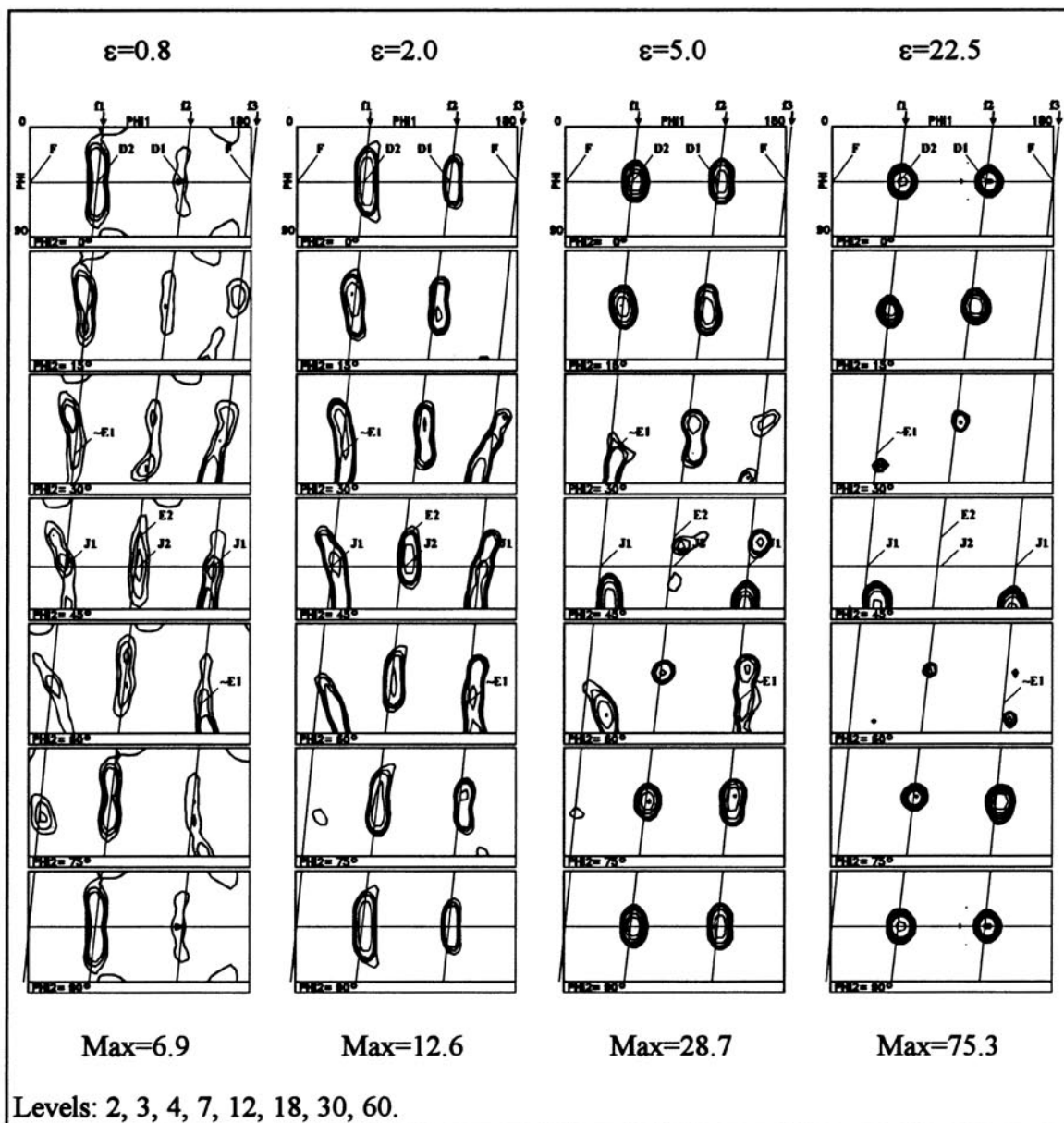
Fig. 20—Simulated ODFs for the oriented nucleation and uniform growth case. RC and shortening (2 pct) conditions (e_{23} component relaxed, $\alpha_s = \alpha_h = 0.95$, $\Delta\gamma = 0.05$, and $\Delta\gamma_{DRX} = 0.25$).

ure 7(a)). Here, the flow curve is very nearly horizontal over the whole steady-state range; *i.e.*, the positive rates of work hardening evident at RT and somewhat higher temperatures decrease to zero at 600 °C. Negative slopes appear only when the temperature is increased beyond 600 °C. This leads to a stress peak at $\varepsilon = 0.6$ at 700 °C (Figure 7(a)); the maximum moves toward the stress axis upon further temperature increases, reaching a strain of 0.4 at 840 °C.

The texture and flow curve trends described previously for the Ti IF steel apply, in a general way, to the Ti-Nb IF steel as well. However, the 600 °C boundary behavior of the Ti IF steel is not reproduced in the latter case. It is evident from Figure 7(b) that the 600 °C curve of the Ti-Nb IF steel is not completely horizontal at large strains and the work hardening rate is still positive (although close to

zero). This indicates that the transition is retarded by the presence of niobium. A maximum followed by flow softening is clearly observed on the 700 °C curve; the transition temperature in the Ti-Nb IF steel can, therefore, be approximated as 650 °C.

Additional experiments revealed that the textures produced at 400 °C, 500 °C, and 600 °C just prior to failure ($3.1 < \varepsilon < 3.6$) resemble the RT texture corresponding to a fracture strain of 3.6. The ODF maxima do not differ significantly from the RT case, and the transition texture is only formed at temperatures above 600 °C. This supports the view that DRX is retarded in the Ti-Nb IF steel, and is consistent with the conclusions drawn from the $\sigma - \varepsilon$ curves of this material.

Similar experiments carried out on the α-iron samples confirmed that DRX begins *earlier* in this material than in

the Ti IF and Ti-Nb IF steels. The α-iron DRX texture at 840 °C is already well developed at a strain of 1.6, with a density maximum of 24.2 at the D2 orientation. Such a strong DRX texture was not observed in the Ti IF steel at the same temperature and at a slightly larger strain of 1.9 (Figure 12). The intensity maximum at the D2 orientation is 14.1 in this case, which decreases further to 11.4 for the Ti-Nb IF steel under the same conditions. Thus, it appears that the transition temperature is about 550 °C in the α-iron.

B. *Continuous DRX*

Continuous DRX is associated with the type of flow curve and microstructure observed in the present experiments. These contrast sharply with the ones produced by the discontinuous mode of DRX. The present flow curves were smooth and exhibited only one gentle maximum (Figures 7(a) and (b)). No oscillations (the multiple peaks associated with the discontinuous type of DRX[35,38]) were evident at any testing temperature in any of the three ferrous materials.

The conclusion that *continuous* DRX was taking place is further supported by the microstructural observations made on the two IF steels and on the α-iron. The type of nucleation associated with discontinuous DRX occurs at existing grain boundaries and is often referred to as a ''necklace'' mechanism. This was not observed in the present work. Instead, the new grains were uniformly distributed (rather than being formed exclusively at the original grain boundaries), as shown in Figures 8(c) through (f), and equiaxed microstructures were formed at strains of about 2.0. They remained essentially unchanged over the entire range of steady-state strains.

The present observations are similar to those described by Montheillet[39] for the high-temperature, high-strain deformation of aluminum. They are also consistent with the work of Dillamore *et al.*[40] carried out on α-iron and two commercial low-carbon steels; the authors concluded that ''the most likely nucleation process is that of subgrain growth, no grain boundary nucleation events having been observed.''

C. *DRX Textures*

It is clear from the experimental textures (Figures 10 through 13) that no new orientations (beyond those already present in the deformation texture) appear when the temperature is increased or when the strain is increased at 840 °C. Some components are, however, strengthened (D1/D2 and E1/E2), while others are weakened (F and J1/J2) and disappear altogether. Such behavior can be understood in terms of the formation of low–Taylor factor (Figure 14) nuclei, followed by the growth of these grains into the matrix. That is, the DRX textures observed in the present materials can be accounted for by the operation of the low-stored-energy nucleation mechanism. Subsequent growth of the nuclei is then uniform (not selective), as indicated by the simulations presented in Figures 19 and 20.

It is not surprising that the oriented nucleation mechanism dominates during the continuous DRX of the α-iron and the two IF steels studied in this investigation. A similar conclusion was drawn by Dillamore *et al.*[40] regarding the

conventional static recrystallization of α-iron and two commercial low-carbon steels, as well as by Kestens and Jonas[36] regarding the static recrystallization of an electrical steel. In the latter case, the main features of the annealing texture were essentially reproduced by assuming that oriented nucleation was taking place. Selective growth was found to play only a minor role and only modified the nucleation texture to a limited degree.

Selective growth also played a minor role in this investigation. Much more satisfactory results were obtained when oriented nucleation was assumed to be followed by uniform growth (compare Figures 19 and 20). The simulation was further improved by applying relaxed constraint, as opposed to full constraint, boundary conditions. Similar relaxed constraint models have often been used in the literature[41,42,43] to improve the correspondence between predictions and observations. In this case, instead of prescribing all the strain components, some were released and allowed to find their own values.

The simulated D1 component is somewhat stronger than that observed experimentally at strains of $\varepsilon = 23.0$ (Figure 12). Such small differences are typical of the uncertainties associated with ODF calculations and texture modeling at large strains. They can be reduced somewhat further by employing ''self-consistent'' as opposed to relaxed constraint methods of modeling. The results obtained in this way will be presented in a future publication.[44]

Nevertheless, the present simulations are sufficiently sensitive to establish the main features of the formation of DRX textures over the experimental strain and temperature range. Because such textures are relatively stable over the steady-state range of flow (compare Figure 13(b) ($\varepsilon = 8.6$, 840 °C) in this work to Figure 5 ($\varepsilon = 21.9$, 840 °C) of Reference 32, for instance), it is clear that the textures developed by DRX persist to large strains (over 20 on the von Mises scale)[32] and that the present simulation results (Figure 20) are representative of the three materials employed in this work. A more recent study[34] has revealed that they also apply to two ferritic stainless steels in which the DRX texture again appears to be produced by the low-stored-energy nucleation mechanism discussed previously.

D. *Retarding Effects of Niobium and Titanium Addition*

Both niobium and titanium retard DRX. This conclusion can be drawn from the present flow curves and DRX textures, as discussed in Section V–A. The retarding effects of niobium and titanium addition are also evident from the softening kinetics of the three materials (Figures 5(a) through (c)). Under the present conditions, postdynamic recrystallization required approximately 30, 80, and 100 seconds in the α-iron, Ti IF steel, and Ti-Nb IF steel, respectively. Thus, DRX is most strongly retarded in the Ti-Nb IF steel, compared to the α-iron, but is still somewhat retarded in the Ti IF steel.

VI. CONCLUSIONS

1. When α-iron, a Ti IF steel, and a Ti-Nb IF steel are deformed in torsion, the work hardening rate (at a given strain) decreases with temperature, eventually leading to

an extended steady-state of flow. This occurs at 550 °C in the α-iron, at 600 °C in the Ti IF steel, and at 650 °C in the Ti-Nb IF steel. A stress peak appears on the flow curve when the temperature is increased beyond these limits. This is followed by a slight decrease in the flow stress with increasing strain.

2. Below the transition temperatures, the large-strain textures of the three experimental materials consist of three characteristic fibers—f1, f2, and f3. The most important fiber components are the F (110)[001], J1 ($0\bar{1}1$)[$\bar{2}11$], J2 ($1\bar{1}0$)[$\bar{1}12$], D1 ($11\bar{2}$)[111], D2 ($\bar{1}12$)[111], E1 ($01\bar{1}$)[111], and E2 ($0\bar{1}1$)[111], listed in decreasing order of importance.

3. At 600 °C, the texture of the Ti IF steel differs somewhat from the lower-temperature textures. High densities of the D2 and E2 components are present, which are attributable to the initiation of DRX. All the principal glide components are still clearly evident under these conditions.

4. The DRX textures of the three experimental materials are primarily composed of the D1 ($11\bar{2}$)[111], D2 ($\bar{1}12$)[111], and E2 ($0\bar{1}1$)[111] components. The D2 becomes increasingly important as the strain is increased; this is accompanied by the weakening of the D1 and the complete disappearance of the E2 at very large strains.

5. The DRX textures observed in the present materials can be accounted for by the operation of the low-stored-energy nucleation mechanism followed by grain boundary migration. The nuclei appear to undergo *uniform* (not selective) growth; thus, oriented nucleation appears to be responsible for the final textures, in the present case, and selective growth can be seen to be relatively unimportant.

6. Continuous (*in situ*) DRX takes place, as multiple peaks were not observed on any of the σ-ε curves determined on the three ferrous materials. The new grains were uniformly distributed and did not form at grain boundaries by a necklace mechanism.

7. The addition of niobium and titanium retards the development of DRX textures and also retards the postdynamic softening kinetics. Under the same conditions, DRX is much more advanced in the α-iron and slightly more advanced in the Ti IF steel than in the Ti-Nb IF steel.

ACKNOWLEDGMENTS

REFERENCES

1. R.D. Doherty: *Met. Sci.*, 1974, vol. 8, pp. 132-42.
2. B. Hutchinson: *Scripta Metall.*, 1992, vol. 27, pp. 1471-75.
3. F.J. Humphreys and M. Hatherly: *Recrystallization and Related Annealing Phenomena*, Pergamon Press, Elmsford, NY, 1995, pp. 206-16.
4. J.E. Burke and D. Turnbull: *Progr. Met. Phys.*, 1952, vol. 3, pp. 220-45.
5. W.A. Johnson and R.F. Mehl: *Trans. AIME*, 1939, vol. 135, pp. 416-58.
6. W.G. Burgers and P.C. Louwerse: *Z. Phys.*, 1931, vol. 67, pp. 605-78.
7. W.G. Burgers and T.J. Tiedema: *Acta Metall.*, 1953, vol. 1, pp. 234-38.
8. J. Hjelen, R. Ørsund, and E. Nes: *Acta Metall. Mater.*, 1991, vol. 39, pp. 1377-1404.
9. C.S. Barrett: *Trans. AIME*, 1940, vol. 137, pp. 128-49.
10. P.A. Beck: *Acta Metall.*, 1953, vol. 1, pp. 230-34.
11. R. Kern, J. Grewen, and H.J. Bunge: *Proc. ICOTOM 7*, Noordwijkerhout, Holland, 1984, pp. 257-62.
12. B.B. Rath: *Proc. ICOTOM 7*, Noordwijkerhout, Holland, 1984, pp. 281-86.
13. K.T. Aust and J.W. Rutter: *Trans. TMS-AIME*, 1959, vol. 215, pp. 119-27.
14. K.T. Aust and J.W. Rutter: *Trans. TMS-AIME*, 1960, vol. 218, pp. 50-54.
15. T. Watanabe: *Proc. ICOTOM 7*, Noordwijkerhout, Holland, 1984, pp. 307-12.
16. W.A. Backofen and B.B. Hundy: *Trans. AIME*, 1953, vol. 197, pp. 61-62.
17. R.O. Williams: *Trans. TMS-AIME*, 1962, vol. 224, pp. 129-39.
18. E. Aernoudt and J. Gil Sevillano: *J. Iron Steel Inst.*, 1973, vol. 211, pp. 718-25.
19. J. Gil Sevillano, P. Van Houtte, and E. Aernoudt: *Z. Metall.*, 1975, vol. 66, pp. 367-73.
20. F. Montheillet, M. Cohen, and J.J. Jonas: *Acta Metall.*, 1984, vol. 32, pp. 2077-89.
21. L.S. Tóth, J.J. Jonas, D. Daniel, and J.A. Bailey: *Text. Microstr.*, 1992, vol. 19, pp. 245-62.
22. J.J. Jonas and L.S. Tóth: *Scripta Metall. Mater.*, 1992, vol. 27, pp. 1575-80.
23. J. Baczynski and J.J. Jonas: *Acta Metall. Mater.*, 1996, vol. 44, pp. 4273-88.
24. S.L. Semiatin, G.D. Lahoti, and J.J. Jonas: *ASM Metals Handbook*, 9th ed., ASM, Metals Park, OH, 1985, vol. 8, pp. 154-84.
25. F. Boratto, R. Barbosa, S. Yue, and J.J. Jonas: *THERMEC-88*, Int. Conf. Physical Metallurgy, Tokyo, 1988, The Iron and Steel Institute of Japan, Tokyo, Japan, 1988, pp. 383-90.
26. P.R. Cetlin, S. Yue, J.J. Jonas, and T.M. Maccagno: *Metall. Trans. A*, 1993, vol. 24A, pp. 1543-53.
27. H.J. Bunge: *Mathematische Methoden der Texturanalyse*, Akademie Verlag, Berlin, 1969.
28. P. Van Houtte, E. Aernoudt, and K. Sekine: *Proc. ICOTOM 6*, S. Nagashima, ed., ISIJ, Tokyo, 1981, vol. 1, pp. 337-46.
29. A. Laasraoui and J.J. Jonas: *Metall. Trans. A*, 1991, vol. 22A, pp. 151-60.
30. G.R. Canova, S. Shrivastava, J.J. Jonas, and C. G'Sell: ASTM STP 753, J.R. Newby and B.A. Niemeier, Eds., ASTM, Philadelphia, PA, 1982, vol. 753, pp. 189-210.
31. J. Baczynski and J.J. Jonas: *Proc. ICOTOM 11*, September 16-20, 1996, Xi'an, China, International Academic Publisher, Beijing, China, 1996, vol. 1, pp. 248-53.
32. J. Baczynski and J.J. Jonas: *Proc. 3rd Int. Conf. on Recrystallization and Related Phenomena*, Monterey, CA, 1996, Monterey Inst. of Advanced Studies, Monterey, CA, pp. 339-46.
33. J. Baczynski and J.J. Jonas: *Proc. ICOTOM 11*, September 16-20, 1996, Xi'an, China, International Academic Publisher, Beijing, 1996, vol. 1, pp. 387-92.
34. J. Baczynski and J.J. Jonas: *Int. Conf. on Texture and Anisotropy of Polycrystals*, Clausthal, Germany, 1997, in press.
35. F. Montheillet and J.J. Jonas: *Encyclopedia of Applied Physics*, 1996, vol. 16, pp. 205-25.
36. L. Kestens and J.J. Jonas: *Metall. Mater. Trans. A*, 1996, vol. 27A, pp. 155-64.
37. J.J. Jonas and L. Kestens: *Proc. ICGG-II*, Kitakyushu, Japan, 1995, Iron and Steel Institute of Japan, Tokyo, 1995, pp. 155-68.
38. T. Sakai and J.J. Jonas: *Acta Metall.*, 1984, vol. 32, pp. 189-209.
39. F. Montheillet: *Les Traitements Thermomécaniques*, INSTN, Paris, 1981, p. 57.
40. I.L. Dillamore, C.J.E. Smith, and T.W. Watson: *Met. Sci. J.*, 1967, vol. 1, pp. 49-54.
41. P. Van Houtte: *Mem. Sci. Rev. Met.*, 1985, vol. 82, pp. 57-68.
42. H. Honneff and H. Mecking: *Proc. ICOTOM 5*, Springer-Verlag, New York, NY, 1978, vol. 1, pp. 265-69.
43. U.F. Kocks and G. Canova: *2nd Risø Int. Symp.*, Risø National Laboratory, Roskilde, Denmark, 1981, pp. 35-44.
44. A. Hildenbrand, J. Baczynski, L.S. Tóth, and J.J. Jonas: McGill University, Montreal, unpublished research, 1997.